Microstructure and properties of steel-aluminum Cold Metal Transfer joints

B. Mezrag, Frédéric Deschaux-Beaume, Laurent Sabatier, Bertrand Wattrisse, M. Benachour

Microstructure and properties of steel-aluminum Cold Metal Transfer joints

B. Mezrag[a], F. Deschaux-Beaume[a]*, L. Sabatier[b], B. Wattrisse[a], M. Benachour[c]

[a] *LMGC, Univ. Montpellier, CNRS, Montpellier, France.*

[b] *LMA, CNRS, Centrale Marseille, Marseille, France.*

[c] *Laboratory of mechanical systems engineering and materials, Tlemcen, Algeria.*

* Corresponding author

E-mail address: frederic.deschaux-beaume@umontpellier.fr

LMGC –UMR 5508

Université de Montpellier – CC048

163 rue Auguste Broussonnet

34090 MONTPELLIER, FRANCE

Effect of Cold Metal Transfer welding parameters on metallurgical and mechanical properties of dissimilar steel-aluminum assembling

Abstract

1 mm thick sheets of 6016-T4 aluminum alloy and Zn coated steel were joined in a lap configuration using the Cold Metal Transfer (CMT) welding process with an Al-5Si filler metal and different powers and welding speeds. The formed reaction layer ensuring the bonding between the aluminum melting zone and the steel sheet doesn't exceed 10 μm in thickness, and is composed of an iron-rich Fe-Al intermetallic on the steel side, and a Fe-Al-Si ternary compound on the aluminum weld side. The current waveform producing the lowest mean electrical power gives the most regular welds with lowest porosity in the melting zone. By optimizing the welding speed with this current waveform, the strength of the assembly under monotonic shear-tensile loading can reach 70% of that of the aluminum base material, and its lifetime under cyclic tensile loading exceeds 10^4 cycles for a maximal linear loading of 98 $N.mm^{-1}$ and 10^7 cycles for a maximal linear loading of 42 $N.mm^{-1}$.

Keywords: dissimilar metal joining; arc welding; steel; aluminum; reaction layer; microstructure; mechanical behavior.

1. Introduction

The assembly of steel to aluminum parts by welding remains difficult due to the large difference of their thermo-physical properties leading to the formation of Fe_xAl_y brittle intermetallic compounds at high temperature, as demonstrated by Kobayashi and Yakou (2002). Many authors have studied the formation and growth of these intermetallic

compounds during the contact of liquid aluminum with solid iron, as Bouché et al. (1998) or Bouayad et al. (2003), or during the contact at high temperature between solid steels and aluminum alloys, as Springer et al. (2011). Others authors investigated solid-state welding methods to join aluminum alloys with steels, as electromagnetic impact welding (Kore et al. 2008), ultrasonic welding (Watanabe et al. 2009), friction stir welding (Watanabe et al. 2006, Coelho et al. 2012) or friction stir spot welding (Chen et al. 2012). With fusion welding processes, previous studies conducted by Sierra et al. (2007, 2008a), Yan et al. (2010) and Torkamany et al. (2010) concluded that interaction between liquid steel and liquid aluminum produced large intermetallic compounds in the weld with many cracks. For these reasons, investigations have been mainly focused on braze-welding methods involving only the melting of aluminum part. The thickness of the formed intermetallic layer has a significant effect on the weld resistance that decreases drastically when its thickness exceeds 10 μm according to Dharmendra et al. (2011). This problem has been overcome by Borrisutthekul et al. (2007) and Fan et al. (2011) by controlling the welding heat input to limit the growth of the intermetallic layer. Previous studies of Peyre et al. (2007) and Sierra et al. (2008a, 2008b) have shown that a lap configuration using a low heat-input welding process can be a good solution because it reduces the heat-input at the interface between steel and aluminum. Whatever the welding process, the use of an aluminum filler metal containing Si ($AlSi_5$ or $AlSi_{12}$) limits significantly the thickness of the reaction layer, as discussed for instance by Mathieu et al. (2006) or Song et al. (2009a, 2009b). However, the nature of the reaction layer is only slightly dependent on the chemical composition of the filler metal, as studied by Dong et al. (2012b). It is mainly composed of two phases: Fe_2Al_5 as major component on the steel side and $FeA1_3$ as minor phase on the aluminum side. As demonstrated by Zhang and Liu (2011), the presence of a zinc coating on the steel surface greatly improves the wetting of the molten aluminum

compared to uncoated steels, aluminized steels and stainless steels. According to Mathieu et al. (2007), this wetting improvement, by modifying the joint geometry, have also a beneficial effect on the mechanical strength of the assembly.

The cold metal transfer (CMT) process used in this study is a controlled metal transfer welding process derived from the well-known Gas Metal Arc Welding (GMAW) process. Zhang et al. (2007) have first used it for steel-aluminum joining in order to try to limit the intermetallic growth. Lin et al. (2013) demonstrated such joints obtained with CMT process could reach significant shear strength. Yang et al. (2013) studied the effect of the location of the CMT welding gun on the flaws formed during joining. Cao et al. (2013) used a Taguchi method to study the effect of some CMT process parameters on the shear strength of lap samples. However, the effect of the process parameters on the physical phenomena involved during joining was not discussed.

The present paper investigates the relations between the welding speed and current waveform of the CMT process, and the characteristics of the steel-aluminum assemblies. Microstructural properties of the welds, as well as quasi-static and cyclic mechanical behaviors of the assemblies are analyzed and the optimum parameters giving the best assemblies quality are suggested.

2. Experimental details

Steel-aluminium welds were achieved using 1 mm thick sheets of 6016-T4 aluminium alloy and DC01 zinc coated mild carbon steel, with dimensions of 150 mm x 55 mm. The Zn coating, supposed to improve the wetting of the molten aluminium, had an average thickness of 23 μm. Filler metal selected as welding wire was ER4043 (Al-5%Si) with 1.2 mm diameter. The chemical compositions of these materials are listed in Table 1.

Table 1

Chemical composition (wt.%).

DC01	Fe : balance	C : 0.08	Mn : 0.6	P < 0.045	S < 0.05				
A6016	Al : balance	Si : 1.2	Mg : 0.4	Cu : 0.25	Cr : 0.1	Mn : 0.2	Fe : 0.5	Zn : 0.2	Ti : 0.15
A4043	Al : balance	Si : 5.2	Mg : 0.05	Cu : 0.3	-	Mn : 0.05	Fe : 0.8	Zn : 0.1	Ti : 0.2

The welding was carried out under pure argon (>99%) as shielding gas with a flow rate of 12 l/min. Before welding, steel sheets were cleaned with acetone while aluminum ones were first polished with abrasive SiC paper to remove oxides and then degreased with acetone. Welds were made in a lap configuration where aluminum is placed on the top with a 10 mm wide overlap, as illustrate in Fig. 1. The torch was positioned perpendicularly to the upper surface and the filler wire was placed on the edge of the aluminum sheet.

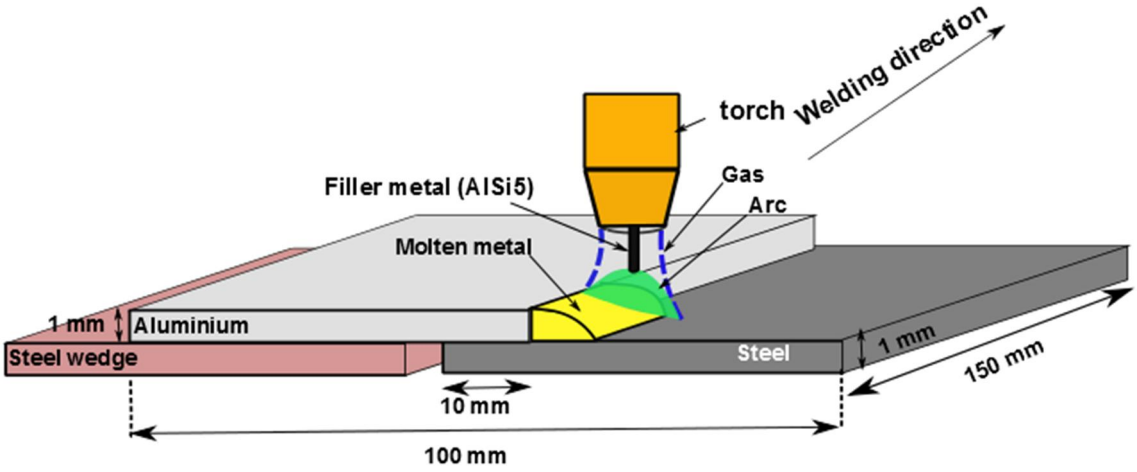

Fig. 1. Shematic representation of steel/aluminium lap welding configuration.

Fig. 2 illustrates the mechanism of metal transfer with the CMT process. It couples an alternating feeding of the filler wire to a precise control of the electrical current waveform that allow the melting and deposit of the filler metal with a minimal heat input. The current pulse (pulse phase) produces a high-energy electrical arc allowing the melting of the filler wire tip. Then, the filler wire is fed towards the aluminum sheet during the "wait phase" under a low arc current until it reaches the sheet, causing a short-circuit and arc extinction.

In this moment, the filler wire retracts up to deposit a liquid metal droplet, producing the arc re-ignition and the next current pulse. Based on our previous experiences of the CMT process (Mezrag et al., 2015), six set of process parameters, corresponding to two current waveforms, were chosen for this study. The first current waveform consists in long pulses with low current (test 1 to 3, Table 2), producing the deposit of large liquid metal droplets with a low frequency, and the second one consists in short pulses with high current (tests 4 to 10, Table 2) producing the deposit of small droplets with a high frequency. The welding parameters chosen for each tests are listed in Table 2.

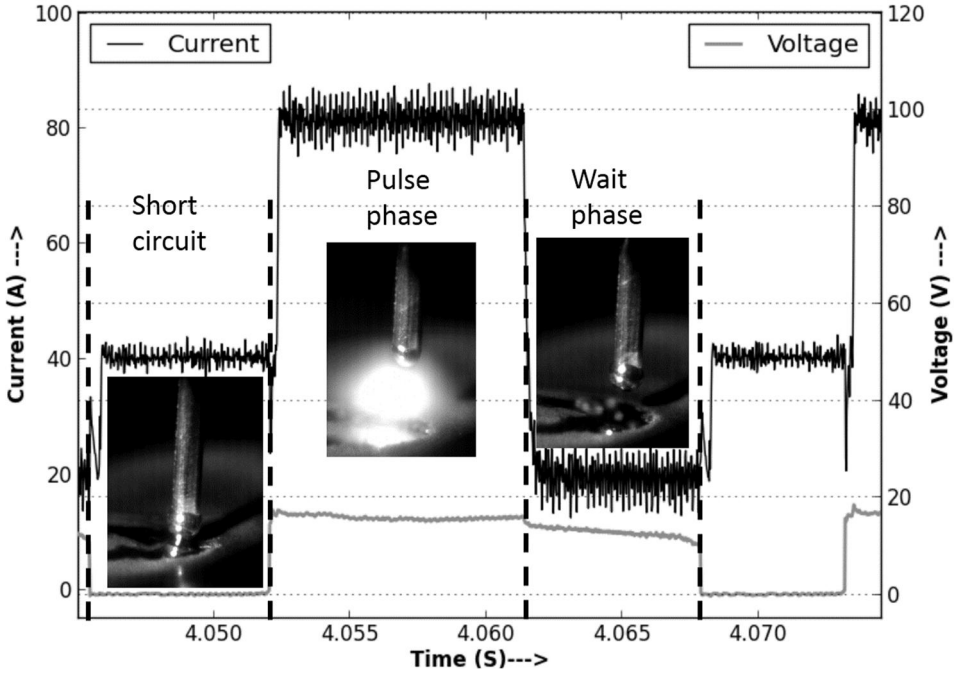

Fig. 2. Metal transfer mechanism with the CMT process

For microstructural characterization, three cross-sections were cut on each sample, and polished using first SiC papers with water lubrication then a diamond paste (6, 3 and 1 μm) to obtain a mirror polishing. To clearly distinguish all the weld zones, the samples were initially etched slightly (3s) with Keller's reagent to reveal aluminum microstructure then for a longer period (10s) with modified Nital (2% HNO_3 diluted in water) to reveal steel microstructure. The prepared specimens were examined using Leica optical microscope

and JEOL 5600 scanning electron microscope (SEM) equipped with energy dispersive X-ray spectrometer (EDS). Some specimens were also analyzed using a CAMECA SX100 Electron Probe Micro Analyser (EPMA) to identify chemical composition of the formed compounds.

Table 2

Welding parameters for the various tests.

N°	Pulse current (A)	Pulse time (ms)	Wait current (A)	Welding speed (cm/min)	Mean power (J/s)	Deposit rate (g/s)	Linear energy (J/mm)
1	64.3	11	17.8	30	570	0.125	114
2	98.5	7	20.7	30	755	0.160	151
3	132.8	3	23.5	30	649	0.162	130
4	150	1.15	28.8	30	399	0.121	80
5	150	1.30	32.6	30	463	0.140	93
6	150	1	25	30	356	0.117	71
7	150	1	25	35	356	0.117	61
8	150	1	25	40	356	0.117	53
9	150	1	25	45	356	0.117	47
10	150	1	25	50	356	0.117	43

Mechanical behavior of assemblies was evaluated in monotonic and cyclic loading conditions using shear-tensile tests described by Peyre et al (2007). In order to confirm the reproducibility of the results, two samples with dimensions of 90x15 mm^2 were cut on each specimen. Mechanical tests were achieved using a MTS servo-hydraulic machine equipped with a 25 kN load cell and data acquisition software. The misalignment of the specimens due to the lap-geometry was compensated by two shims of same thickness as the base material (Fig. 3). Due to the dissymmetry of the specimens, the stress as well as the strain were not uniform in the test samples. For this reason, only the global mechanical behavior of the samples was analyzed, by recording the evolution of the linear force (N/mm) defined as the ratio between the applied force and the weld length (15 mm) versus

the displacement of the movable jaw. The quasi-static experiments were carried out at a displacement speed of 1 mm.min^{-1}. The joint strength was evaluated by the peak of linear force. The fatigue tests were performed under an imposed sinusoidal cyclic loading with a stress ratio R of 0.1 and a frequency of 20 Hz up to failure. Four maximum load levels were selected according to the maximum load (L_{max}) or the load corresponding to the end of the linear domain (L_e) determined on the monotonic tensile curves for the different assemblies: 0.8L_{max}, L_e, 0.7L_e and 0.3L_e. To better understand the mechanisms of initiation and propagation of fracture, high-speed videos were recorded during tests with a PHANTHOM V710 high-speed camera.

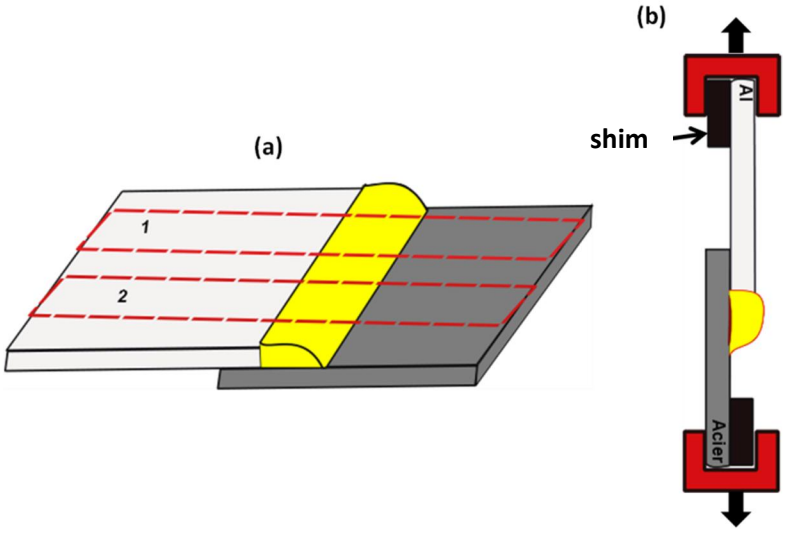

Fig. 3: (a) samples location for the tensile tests and (b) schematic representation of the tensile test

3. Results and discussion

3.1. Visual aspect of the welds

All the welds obtained were regular and free from spatters and macro defects such as cracks, which testify a stable metal transfer and good wetting of molten aluminum. In a general way, welds made with the first current waveform at a welding speed of 30 cm.min^{-1} (tests 1 to 3) were more spread and rough, while those made with the second waveform

(tests 4 to 6) were smoother and narrower. This can be explained by higher mean powers when using first current waveform. The size of the weld pool, estimated from the crater formed at the end of the welding during arc extinction, was very large in the first case, due to high deposition rates, but also to a greater melting of the aluminum sheet. The heating of the steel sheet was limited, as evidenced by the presence of the initial zinc coating on the surface adjacent to the weld as well as on the opposite face for all tests.

For the lowest mean power (tests 6 to 10), when the welding speed increased from 30 to 50 $cm.min^{-1}$, the weld became much narrower but more irregular (Fig. 4.a). This shows a greater difficulty for the liquid filler metal to both melt the base aluminum alloy and wet the steel surface when the speed welding increases.

The contact line between the weld and the steel surface often showed undulations (Fig. 4.b). This shape was attributed by Yang et al. (2013) to the interaction between the zinc vapor formed on the steel surface and the liquid aluminum which can locally modify the wetting.

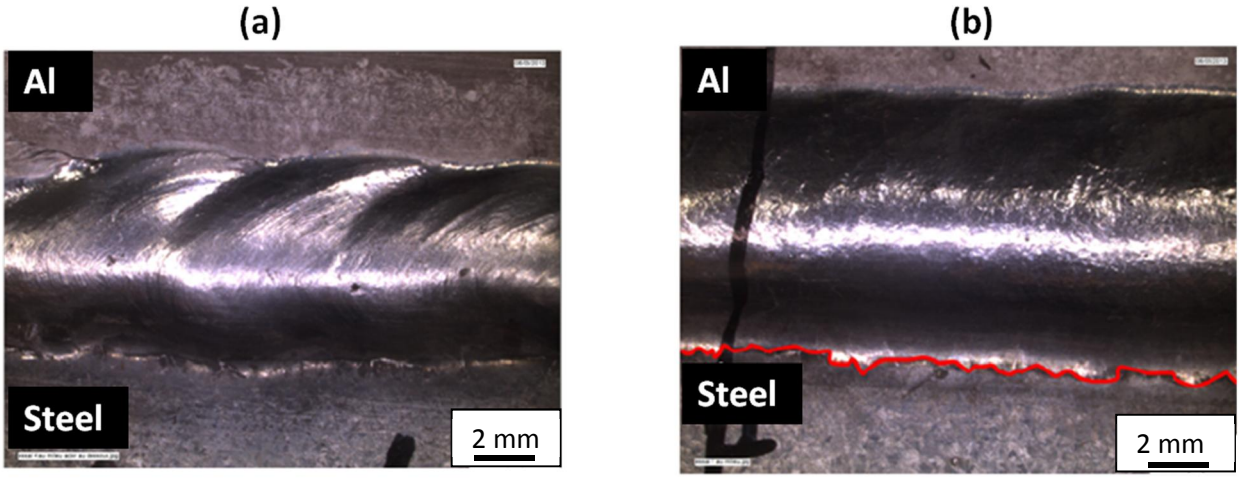

Fig. 4. Visual aspect of the welds: (a) test 9, (b) test 6.

3.2. Macrographs and micrographs of welds cross-sections

Fig. 5 illustrates a typical cross-section of the steel-aluminum assemblies. It can be seen that the weld foot (steel side) has a very low wetting angle (Fig. 4.b), revealing a good wetting of the aluminum on the Zn coated steel surface. Since the melting temperature of the zinc is very low (419 °C), it is generally accepted, as discussed by Peyre et al. (2007) that the liquid aluminum is deposited on a liquid layer of Zn. Numerous micro-porosities have been observed mainly on the upper part of the weld (Fig. 5.c). The weld root was also characterized by systematic formation of a large porosity, located just at the border of the molten zone, or a little inside the weld (Fig. 5.d). These porosities can be attributed to two main factors: the presence of dissolved hydrogen in the liquid aluminum and its rejection during solidification and/or the vaporization of zinc that can occurs above 906°C. The spheroidal geometry and small diameter (<100 μm) of the porosities formed in the upper part of the molten zone suggest that their origin is rather the dissolved hydrogen, which is a frequent cause of porosities in aluminum alloys. Since the solubility of hydrogen in liquid aluminum is about twenty times higher than its solubility in solid aluminium, the supersaturated hydrogen was rejected during solidification in the liquid not yet solidified, and eventually formed spherical gas bubbles when the solubility was exceeded. On the other hand, the presence of high zinc content on the surfaces of the large porosity formed in the weld root demonstrates the role of Zn vapor on the formation of this defect.

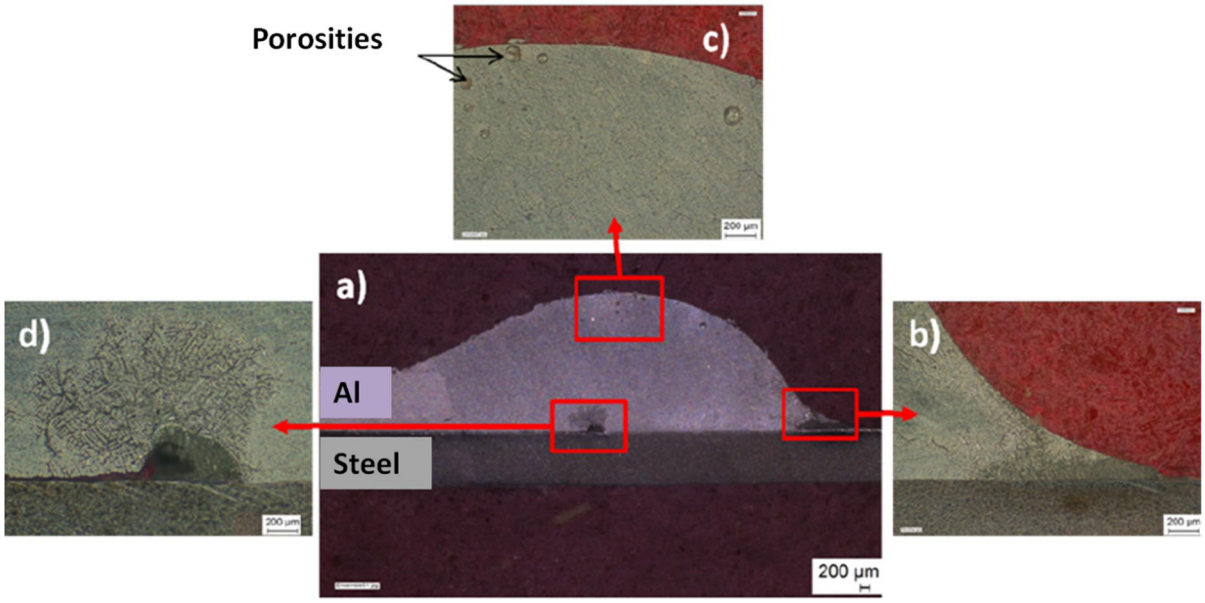

Fig. 5. Typical cross-section morphology of steel-aluminum welds.

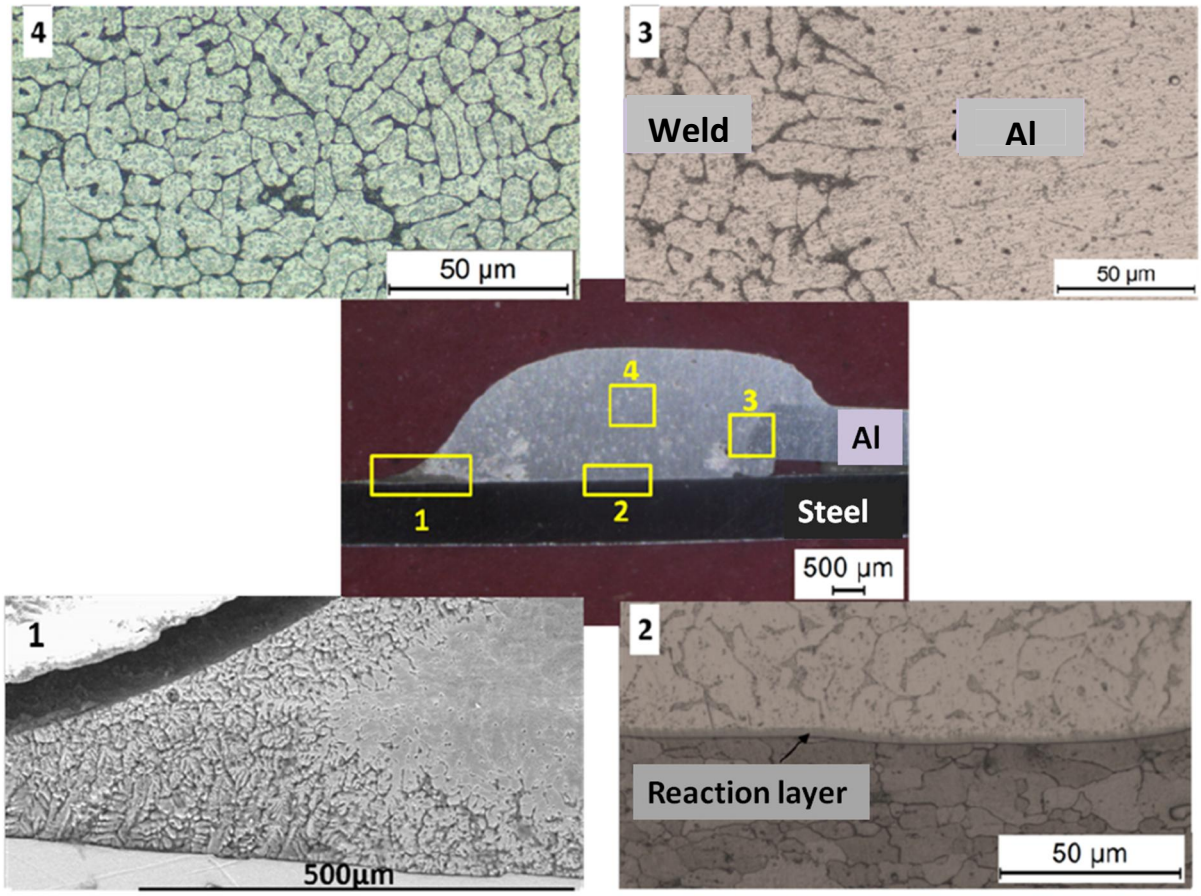

Fig. 6. Micrographs of the main zones of the welds cross-section.

As can be seen in Fig. 6, a thin intermetallic layer was formed at the weld/steel interface with an average thickness in the center of the reaction layer between 2 and 8 µm depending on the welding parameters. The thickness of this layer was not uniform along the interface. It was maximum in the center and decreased in the edges of the weld. Fig. 7 shows the distribution of reaction layer thicknesses along the interface on a cross section taken from the center of the welded samples for tests 1 to 6, performed at the same welding speed of 30 cm.min^{-1}. They reflect the energy distribution transmitted through the interface and show that the current waveforms of tests 4 to 6 formed thinner and more regular reaction layers than the current waveforms of tests 1 to 3. As previous studies of Sierra et al. (2008), Lin et al. (2010), Dong et al. (2012a) or Zhang et al. (2013) have shown, the interface between the reaction layer and the bead had a serrated morphology, whereas the interface was more planar in the steel side. The greater was the average power, the greater were the irregularities with some cracks when the reaction layer thickness exceeded 10 µm, as shown Fig. 8.

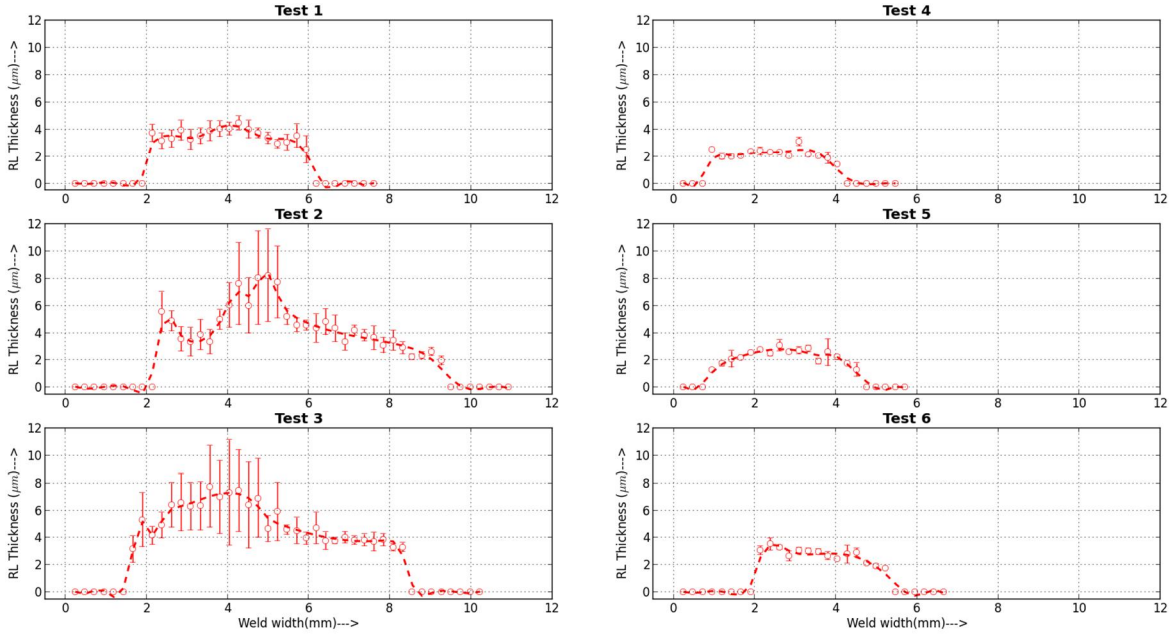

Fig. 7. Distribution of reaction layer (RL) thicknesses along the interface for tests 1 to 6.

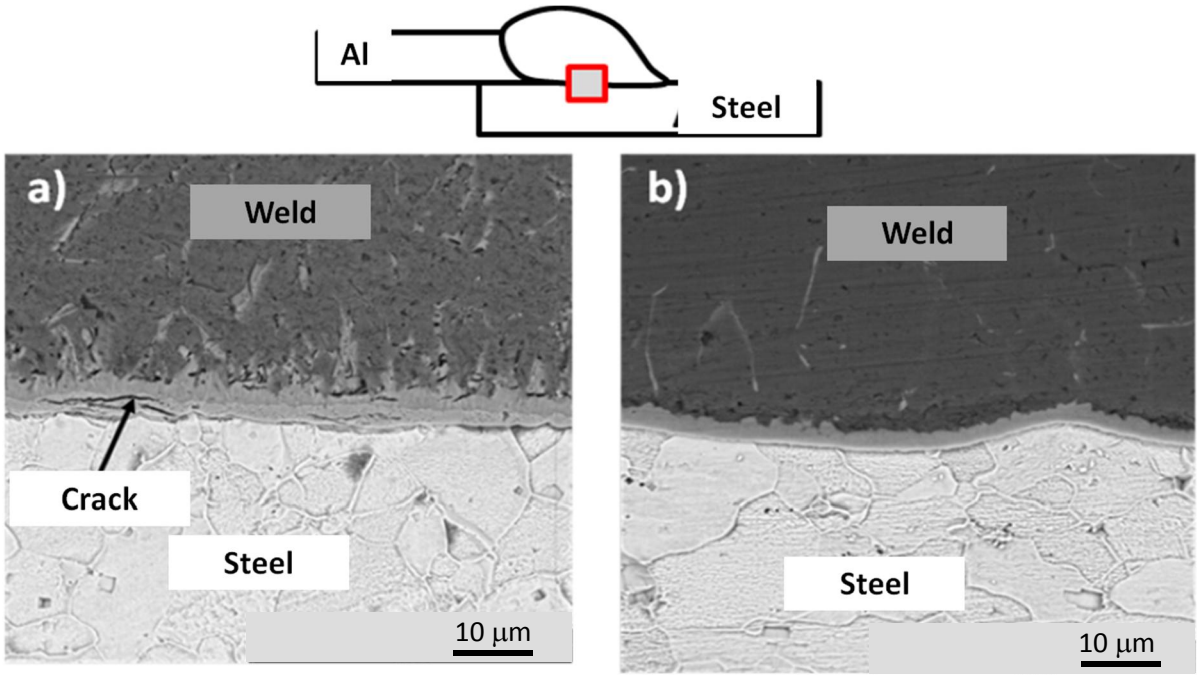

Fig. 8. Comparison of the formed reaction layers for: (a) a high average power, test 2, (b) a low average power, test 6.

3.3. Chemical composition of reaction layers

To determine the chemical composition of the compounds formed in the reaction layer, Electron Probe Micro Analysis (EPMA) were carried out. Fig. 9 shows EPMA profiles giving the compositions evolution of the reaction layers for two assemblies obtained with same waveform and different welding speeds (tests 6 and 10).

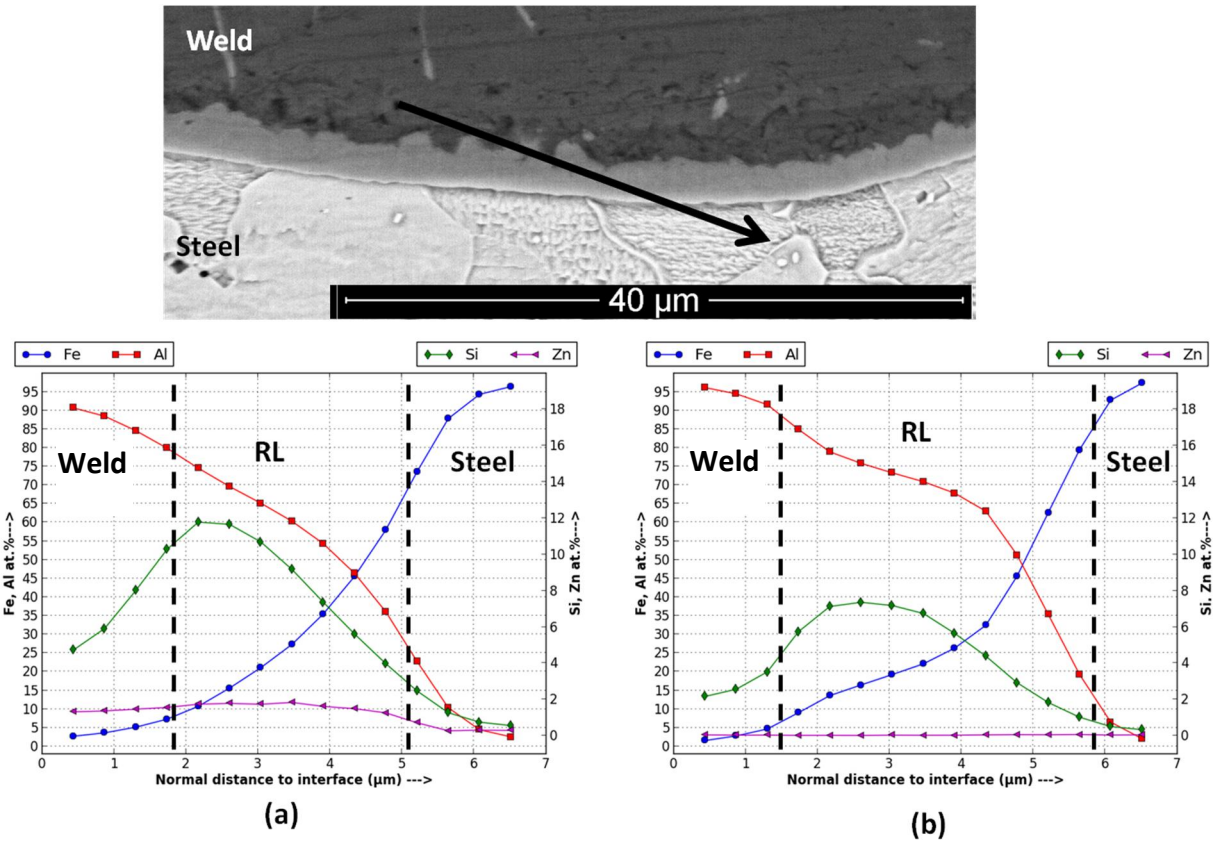

Fig. 9. EPMA analyses of the reaction layer (RL): (a) test 10, (b) test 6.

For both welding speeds, a decrease in the Al content and an increase in the Fe content can be observed in the reaction layer when passing from the weld side to the steel one, which seems to show the presence of different intermetallic compounds. Referring to the composition domains of phase stability of Fe-Al intermetallics given by Shahverdi et al. (2002), it can be assumed the presence of a Fe_2Al_5 or $FeAl_3$ phase on the weld side, and maybe an iron-rich intermetallic phase (FeAl or Fe_3Al) on the steel side. However, there is also a significant silicon content (up to 12 at%) in the weld side of the reaction layer. It is also noted that the silicon content is higher in the reaction layer than in the weld, whereas this element comes from the filler metal. It appears therefore that the intermetallic formed during the contact of the liquid aluminum with the surface of the steel is a Fe-Al-Si ternary

compound, presumably the $Fe_2Al_{7.4}Si$ phase already encountered by Raghavan (2009) (71.25-68.75 Al at. % -18.75 Fe at. % -10-12.5 Si at. %).

There is a gradual decrease in the Si content in the reaction layer as we approach to the interface with the steel. We can then assume the formation of two distinct types of intermetallic, an Fe-Al-Si intermetallic on the Al side, and Fe_2Al_5 or an iron-rich compound on the steel side. The higher Si content in the reaction layer formed with the higher welding speed (Fig. 9a) confirms this assumption. The two phases were presumably formed at the same time during the contact of liquid aluminum with steel surface, and then the reaction layer on the weld side was partially dissolved in the liquid phase. This dissolution was greater as the interaction time is long, which is the case when the welding speed is slower, that explain the lower content of Si in the reaction layer in this last case. In the case of high welding speed, a significant Zn content (close to 2 at. %) was also observed in the reaction layer and the weld near the interface, which indicate its low evaporation **due to a lower linear energy.** However, no zinc was observed in the reaction layer for slower welding speeds. This result was explained by Zhou et al. (2014) by the low miscibility of liquid aluminum and liquid zinc. The molten Zn was then pushed back towards the weld foot that allow the direct wetting of liquid aluminum on steel surface when interaction time is long enough.

3.4. Mechanical characterization

3.4.1. Quasi-static monotonic shear-tensile behavior

The behavior of the assemblies during shear-tensile tests was compared to the mechanical behavior of the parent material 6016-T4 during tensile test on samples of similar sections, which support a maximal tensile loading of 294 $N.mm^{-1}$. Only samples 1, 3, 6, 8 and 10 were characterized using shear-tensile tests. Samples 1, 3, 6 were obtained using the same

welding speed of 30 cm.min^{-1} but various heat inputs, whereas samples 6, 8, 10 were obtained using the same heat input but various welding speeds.

Three kind of behavior were observed (Fig. 10). All the samples achieved at the welding speed of 30 cm.min^{-1} (samples 1, 3 and 6) showed similar tensile curves and fracture behavior, so only the curve of sample 6 is shown on Fig. 10.

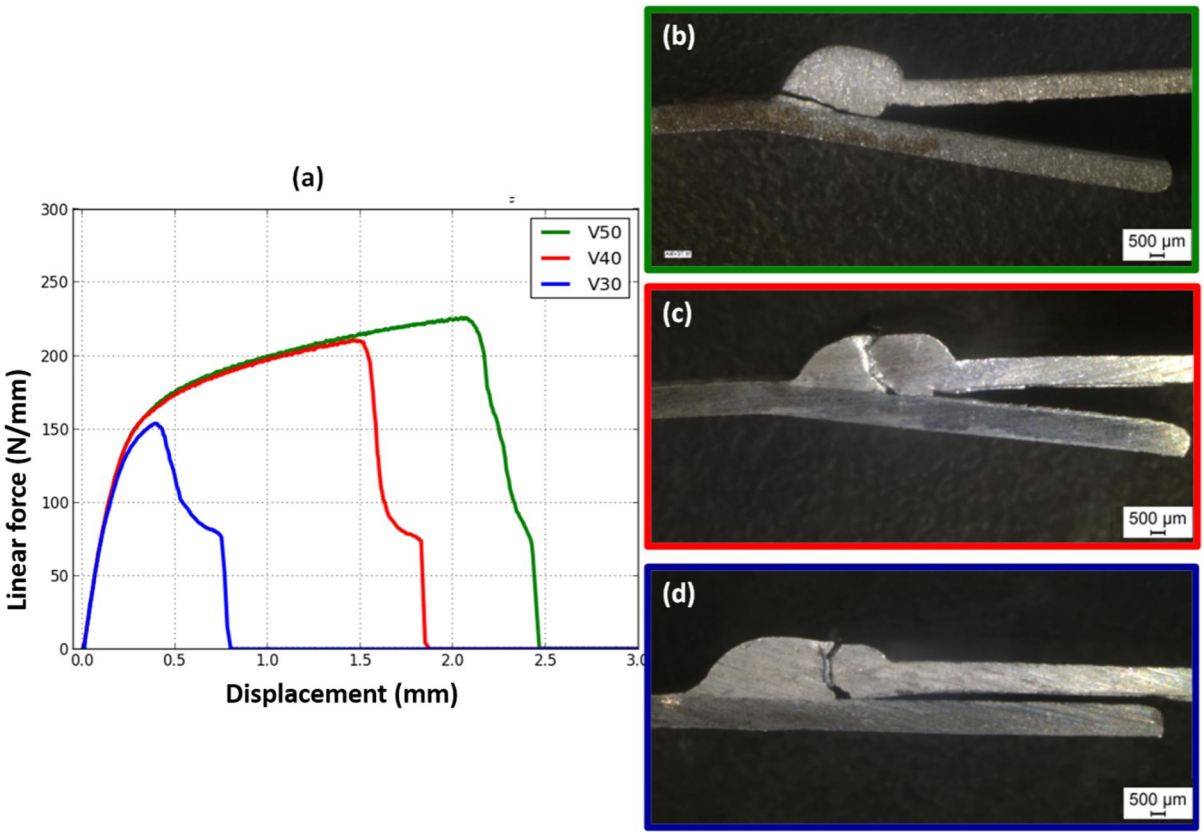

Fig. 10. (a) Tensile curves, and fracture location in assemblies made with welding speed of (b): 50 cm.min^{-1}, (c): 40 cm.min^{-1}, (d): 30 cm.min^{-1}.

The assemblies are designated according to their welding speed (30, 40 and 50 cm.min^{-1}, see table 2): V30, V40, V50. The tensile curves (Fig. 10.a) show rather similar linear parts, which indicates similar rigidities of the three assemblies. The non-linear part starts a little earlier for the lowest welding speed, revealing an early plastic strain compared to the other samples. In this case, the fracture occured at a lower loading level, equivalent to only 53%

(155 $N.mm^{-1}$) of the strength of 6016-T4 aluminum alloy. The low displacement observed on this curve indicates the plastic strain was rapidly localized in the zones of high stress concentrations and/or the cracking started very early. The observation of the broken samples showed that fracture initiated in the weld root and then propagated in the molten zone (Fig. 10.d). The high-speed video recorded during the test (Fig. 11) confirmed the cracking mechanism. Under the effect of the asymmetrical loading of the bonding interface, this one undergone a slight rotation increasing the stresses concentration in the root zone causing a crack initiation on the large porosity attributed to the zinc vaporization, estimated on micrographs and fractographies to about 150 to 200 μm diameter. The crack propagated then in the weld perpendicularly to the tensile axis.

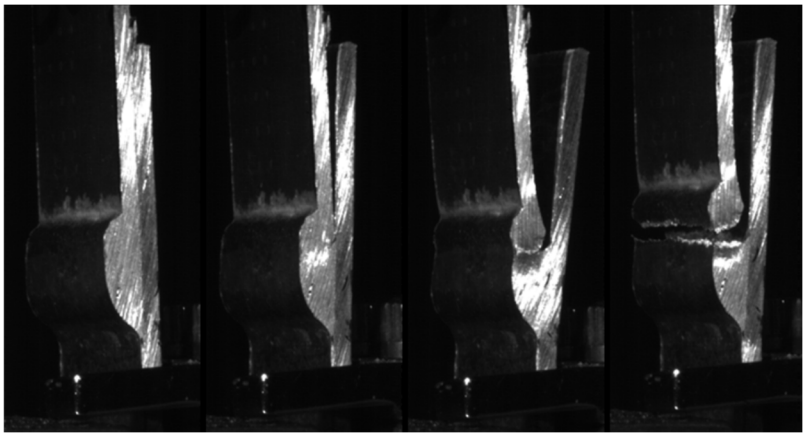

Fig. 11. High-speed video images of the shear-tensile test showing the rotation of the sample V30 during the test and the crack initiation and propagation.

Fractographic analysis showed that the cracks follow a network of fine porosities formed in the weld, and the presence of dimples indicating a ductile fracture mode (Fig. 12).

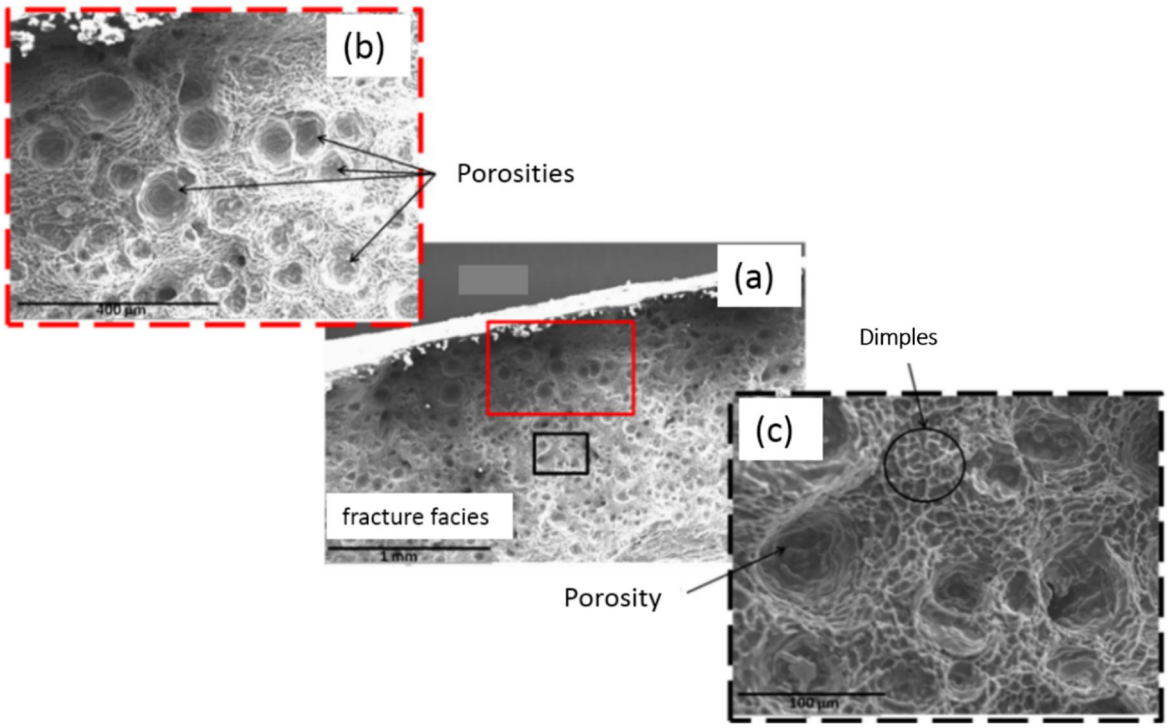

Fig. 12. SEM observations of the fracture facies of theV30 assembly.

The assemblies made at 40 cm.min^{-1} and 50 cm.min^{-1} had tensile curves with a longer non-linear part and the fracture occured for higher loads and displacements (Fig. 10.a).

The high-speed video showed the cracking started always at the weld root, but after a greater rotation of the bonding interface than the first case (Fig. 13). For V40 specimens, the crack propagated along the interface then deflecting in the molten zone perpendicularly to the direction of the tensile axis, when it encountered a large porosity at the interface.

The fracture took place under loading levels corresponding to about 70% of the strength of the 6016-T4 aluminum alloy. The crack deviation was not observed in the case of V50 assemblies, certainly because of the small size of the porosities in the molten zone, estimated on micrographs to about 60 µm diameter, compared to about 100 µm diameter for V40 assemblies. In this case, the fracture propagated along the steel/weld interface, leading to the highest linear strength, equal to 76% of the strength of 6016-T4 aluminum alloy.

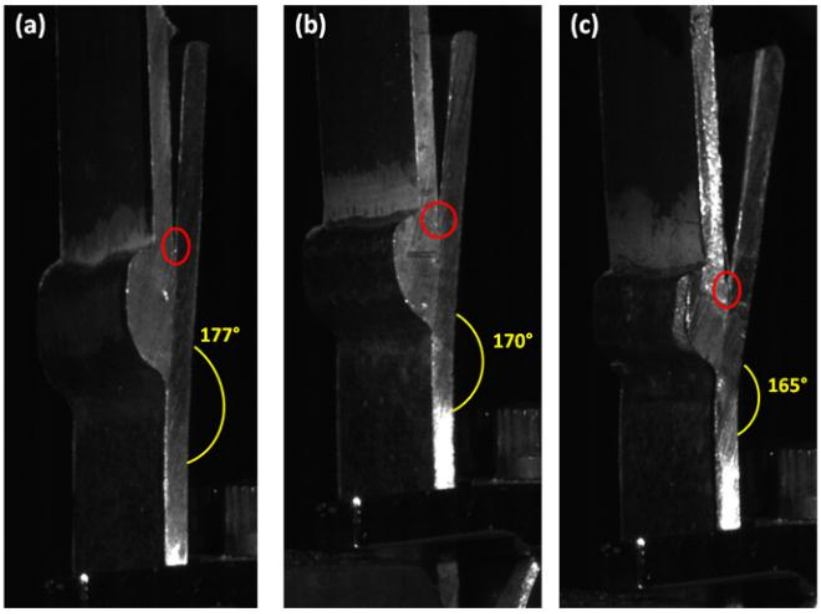

Fig. 13. Rotation of the bonding interface at the time of crack initiation (in red circle) for assemblies (a): V30, (b): V40 and (c): V50.

Fractographies of the interfacial rupture zones obtained with V50 samples (Fig. 14) showed large flat areas characteristic of brittle fracture. The EDS chemical analysis (Table 3) on the weld side of the fractured surfaces revealed very low iron contents (maximum 4 at. %), which indicates that the fracture propagated mainly into the reaction layer very near the interface with the weld. The EDS analysis of the fracture surface on the steel side revealed very different chemical compositions in the root and the foot of the weld. On the root side, where the crack initiated, the fracture surface had high Fe and Al contents, as well as silicon, which indicates the crack propagated first through the intermetallic layer. While near the weld foot, Fe content became very low and the Zn content increased, which show that the crack deviated in the weld, although the fracture facies retained a brittle aspect.

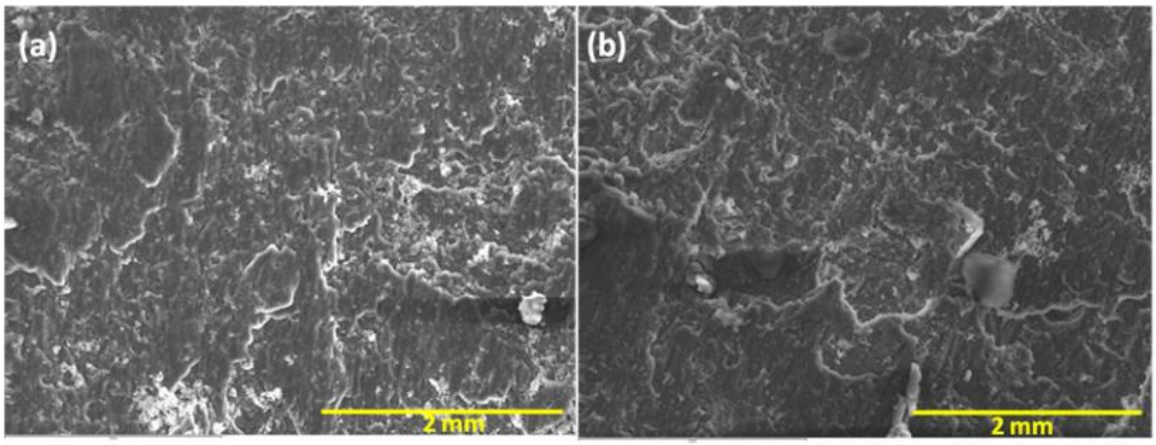

Fig. 14. SEM micrographs of the fracture facies of V50 samples, (a): steel side, (b): aluminum side.

Table 3

EDS analyses of various area of the fracture surface of V50 samples

at. %	**Fe**	**Al**	**Zn**	**Si**
Weld side	0.5-4	55-76	4-26	10-14.5
Steel side (root)	60-67	24-32	6-12	0.5-1.5
Steel side (foot)	0.5-6	55-82	15-24	2-11

These results show a change of the fracture mechanism and the strength levels of the assemblies as a function of welding speed. The fracture mechanism depends mainly on the size of the porosity formed in the weld/steel interface. In all cases, the fracture initiated in the weld root, due to the stress concentrations produced in this zone, accentuated by the rotation of the bonding interface. The propagation of the crack then occured, depending on the case:

- In the weld, perpendicular to the tensile direction in the case of low welding speed producing very large porosity at the weld root;

- Along the bonding interface if there was no large root porosity, until the crack encountered a large porosity at the interface which cause its deflect in the weld, perpendicular to the tensile axis;

- Along the bounding interface until complete separation of the specimen, when the welding speed was higher (i.e. the linear energy was lower) and did not produce large porosity in the melting zone.

The strength of the assemblies thus depends mainly on the size of the defects formed in the molten zone near the interface, which itself depends on the welding linear energy: the higher is the linear energy, the greater is the porosity size, and the lower is the strength of the assemblies.

3.4.2. Fatigue behavior

The three assemblies 6, 8 and 10 characterized under quasi-static loading were also tested under cyclic tensile loading. Four levels of maximum loading, summarized in table 4, were chosen as a function of the maximum linear force (L_{max}) or the linear force (Le) corresponding to the end of the linear domain of monotonic shear-tensile tests.

Table 4

Linear forces in monotonic shear-tensile tests and maximum loading levels retained for fatigue tests for the different tested assemblies.

	V30	**V40**	**V50**
L_{max} (N.mm^{-1})	156	210	228
L_e (N.mm^{-1})	140	140	140
Level 1 (0.3L_e)	42	42	42
Level 2 (0.7L_e)	98	98	98
Level 3 (L_e)	140	140	140
Level 4 (0.8L_{max})	125	170	180

Fig. 15 illustrates the raw curve obtained for cyclic tensile test on a V50 sample tested with maximal loading (level 4). The imposed sinusoidal cyclic loading was the setpoint to respect by adjusting the travel speed of the hydraulic cylinder of the machine. As a high 20 Hz cycle

frequency was also imposed, the loading setpoint was not respected for the first cycles, due to the progressive accommodation of the travel speed. Hence the maximal load imposed was reached only after about ten to twenty cycles. Several cycles were still needed to reach the stabilized hysteresis loop. Then, after a certain number of stabilized cycles, the maximal load rapidly decreased due to the crack propagation leading to the sample fracture. In order to compare the results obtained for the different assemblies and test conditions, the outer envelope joining the highest load level of each cycle was extracted from the recorded data (red points on Fig. 15).

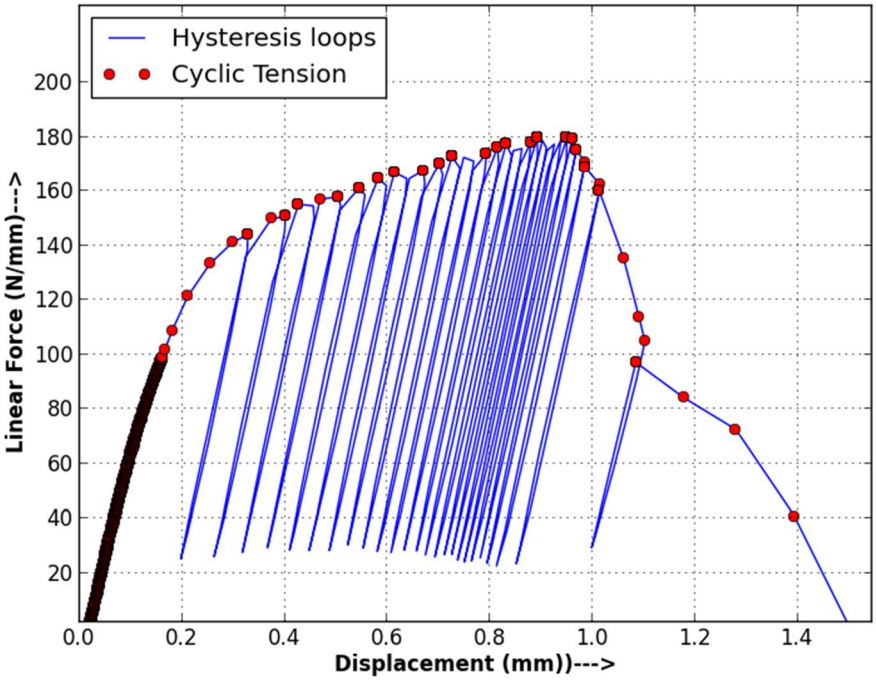

Fig. 15. Cyclic tensile curve for sample V50 and level 4 of maximal loading.

The cyclic tensile curves obtained under different loads for each assembly (Fig. 16) showed that the linear parts of the curves superimpose perfectly for all the assemblies and loading levels, which indicates that they have the same linear behavior. The curves obtained with level 1 maximal loading (0.3Le) are not presented because the fracture did not take place in this case before 10^7 cycles. The displacement at the beginning of the

crack propagation d_{max}, detectable by the first decrease of the maximal load of the loop, increases with the maximum loading.

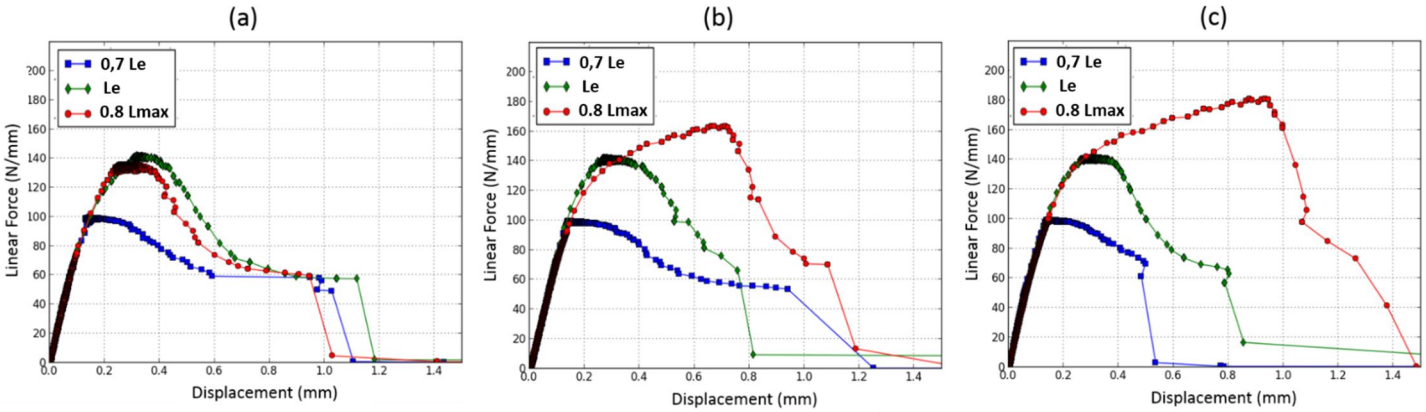

Fig. 16. Cyclic tensile curves of the assemblies under different maximum loads: (a) V30, (b) V40, (c) V50.

When superimposing the cyclic tensile curves carried out under the same loading level for the three assemblies (Fig. 17), a very good superposition is also observed until the fracture. This indicates that the plastic strain localization and the damaging mechanisms were similar for the three assemblies. Finally, it can be noted that in all cases, fracture occured after a relatively large displacement.

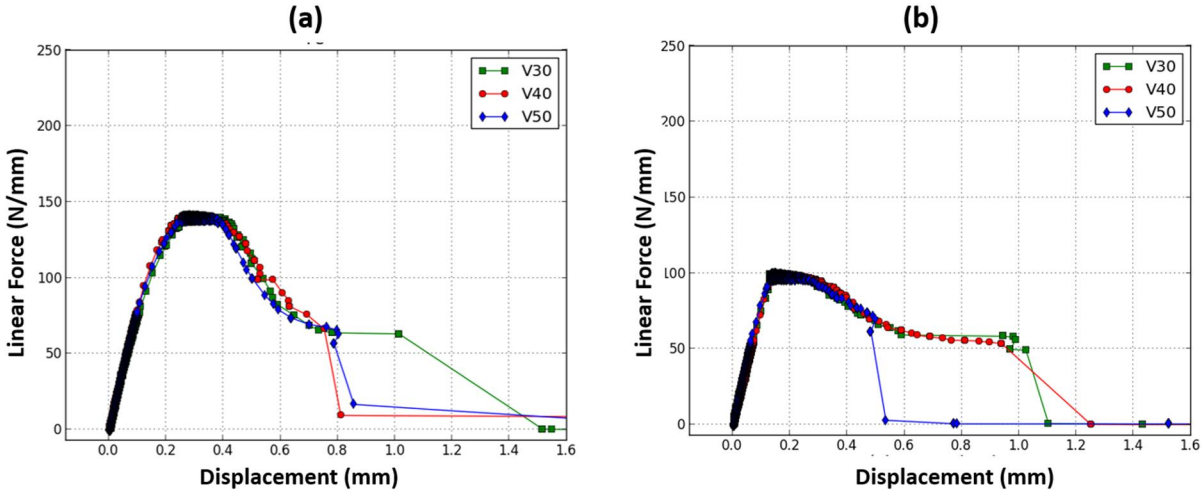

Fig. 17. Cyclic tensile curves of the three assemblies under a maximal loading of (a) Le, and (b) 0.7Le.

The evolution of the maximum displacement as a function of the number of cycles, shown in Fig.18, can be divided into three distinct stages:

- During the first stage, the displacement increases rapidly, due to the progressive increase of the maximum loading during the first cycles but also to the accommodation effect, until a stabilized cycle is reached;

- In the second stage, the hysteresis loop stabilizes, and the maximum displacement evolves very slowly. The duration of this stage was longer as the maximum loading imposed was lower, and varied with the welding speed. This stage was not observed for tests carried out with a maximal loading of $0.8L_{max}$;

- The final stage corresponds to an increase in the maximum displacement at each cycle. This stage is associated with the initiation and propagation of a macroscopic crack until the fracture of the sample.

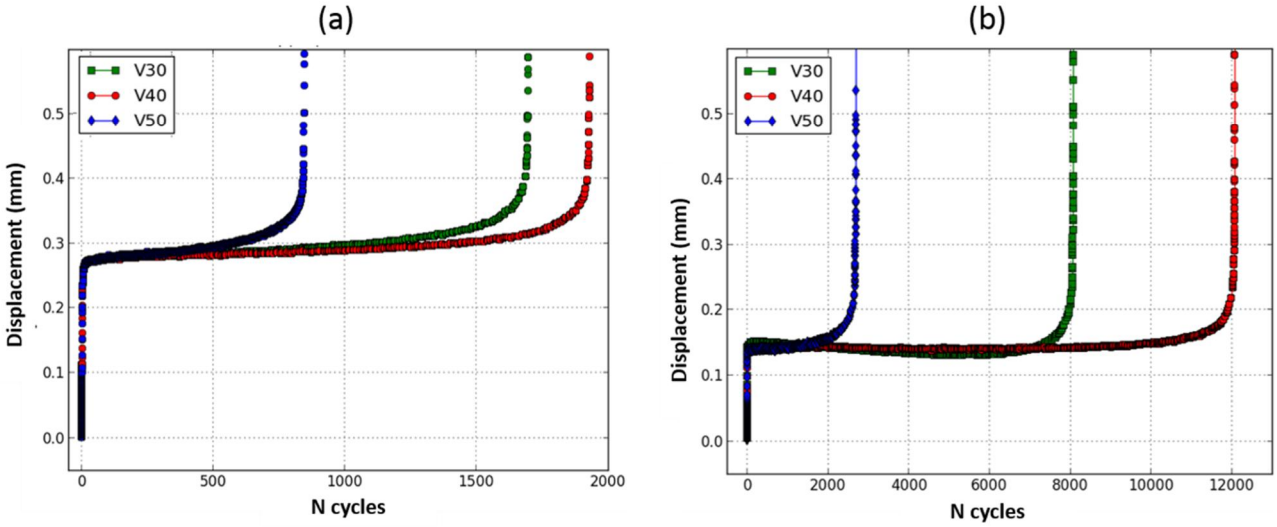

Fig. 18. Evolution of the displacement as a function of the number of cycles during the fatigue tests under a maximal loading of (a) L_e and (b) $0.7L_e$.

Fig. 19 gives the S-N curves representing the evolution of the maximal load of the fatigue cycle as a function of the number of cycles to fracture for the tested assemblies. Despite

some dispersion, probably due to the random nature of the internal defects distribution (porosity) in the specimens and to some variation in weld geometry for similar welding parameters, this figure shows a better fatigue behavior of the V40 and to a less extent V30 assemblies compared to the V50 assemblies, which nevertheless exhibited the best monotonic tensile behavior. Fig. 19 shows the lifetime under cyclic tensile loading of V40 assemblies exceeds 10^4 cycles for a maximal linear force of 98 $N.mm^{-1}$.

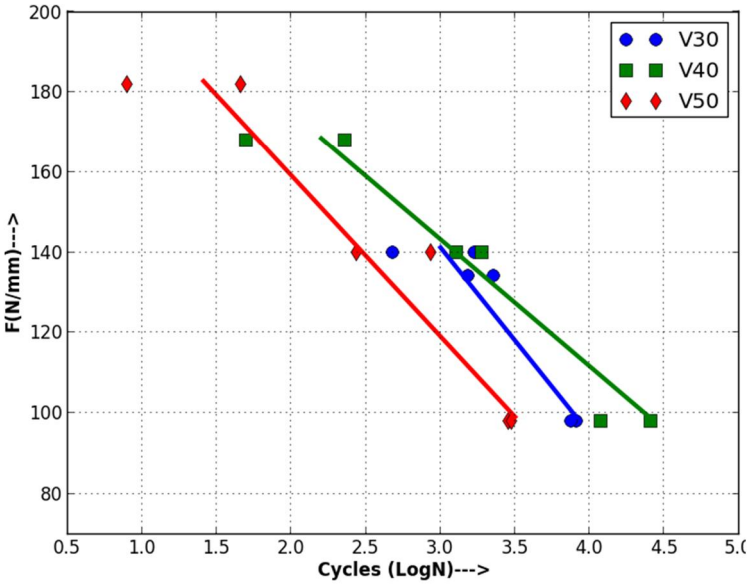

Fig. 19. S-N curves for the different assemblies.

Fig. 20 shows the fracture location in the tested assemblies under different cyclic loadings. In all cases, the fracture systematically initiated at the weld root, propagated first along the weld/steel interface, and then deviated in the weld. This suggests that the reaction layer had a rather good toughness since the crack deviated into the weld instead of its propagation throughout the reaction layer. The high-speed videos recorded during the cyclic tensile tests confirmed that all samples are cracked from the weld root, which was the weakest zone in the steel/aluminum assembly in lap configuration. The crack deviation from the interface towards the weld center can be attributed to the presence of large porosities due to the Zn evaporation, as observed in monotonic tensile tests. This crack deviation could be

associated to the acceleration of the maximal displacement increase in the late stage of the test observed in figure 18.

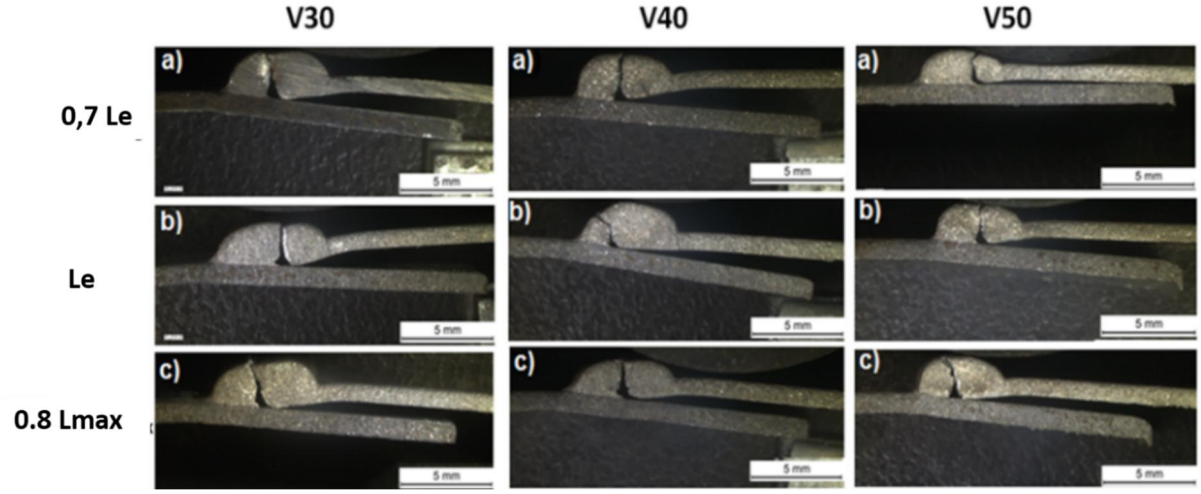

Fig. 20. Location of fatigue failure of assemblies under different maximal loads.

For all broken samples, scanning electron microscopy of the failure facies showed the existence of two distinct areas (Fig. 21). Zone 1 corresponds to the crack initiation area near the root of the weld. It has a brittle aspect, consistent with its location in the reaction layer. Zone 2 presents a ductile facies and corresponds to the propagation of the cracks in the weld. A large number of porosities was also observed on all the facies, dispersed over the whole of the fracture facies.

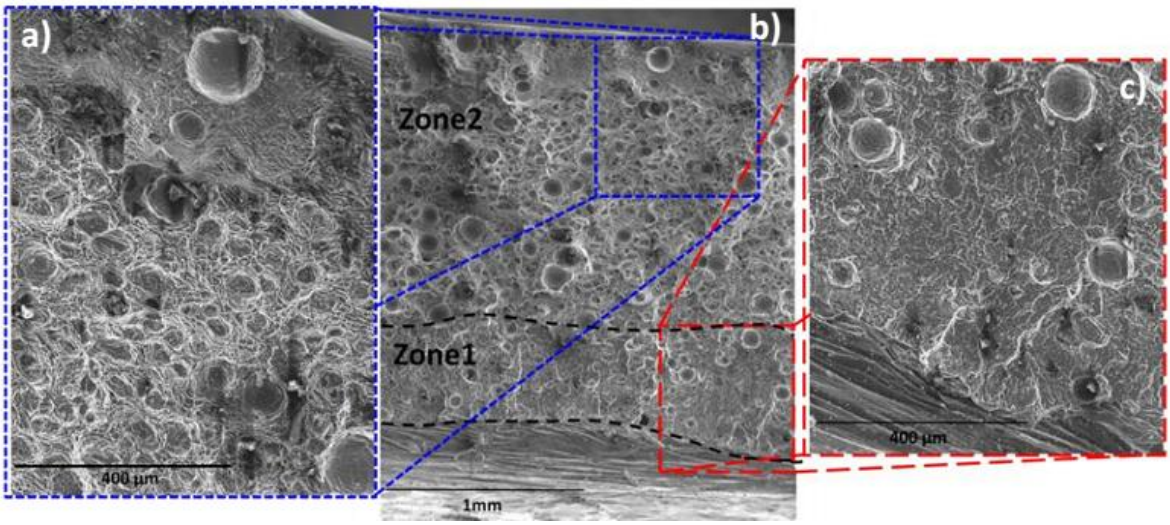

Fig. 21. Aspect of the fracture facies after fatigue failure, showing the crack propagation zone along the interface (zone 1, (c)) and the crack propagation zone into the weld (zone 2, (a)).

The mechanism of fatigue failure appears to be identical to the one observed under monotonic shear-tensile loading for samples V30 and V40. Under the effect of the stress concentration in the weld root, the plastic strain was localized in this zone, leading to the initiation and propagation of a crack along the bonding interface and then in the weld. The presence of large interfacial porosity and the porosity in the melting zone favors the crack deviation into the weld, by reducing the real section of the specimen in the melting zone and creating additional stress concentrations. The presence of a large amount of porosity in the V30 assemblies can thus explain that they are less fatigue resistant than the V40 assemblies. The lower fatigue strength of the V50 assemblies compared to V40 is more difficult to explain. Contrarily to the other samples, there is a change in fracture mechanism in this case, with a crack propagation through the reaction layer in monotonic shear-tensile tests, and a propagation into the melting zone in fatigue tests. It can be related to the more harmfull effect of the interfacial porosity in cyclic loading, and to the smaller molten zone, which reduce its resistance. At the opposite, the presence of some

very small porosities in V40 molten zone can act as a loading damper that explain its better fatigue strength.

4. Conclusions

Zn coated DC01 steel and 6016-T4 aluminum sheets were welded in a lap configuration with an Al-5Si aluminum filler metal with different current waveforms using the CMT welding process.

For all assemblies, two types of defects were observed in the welds: fine and dispersed porosities localized mainly in the upper part of the welds, attributed to the dissolution of hydrogen in the liquid aluminum, and large porosities located near the weld root, attributed to the zinc coating vaporization. The size of these defects increases with the welding power.

The weld/steel bonding is provided by an interfacial reaction layer, constituted of a Fe_2Al_5 or iron-rich Fe-Al phase with variable silicon contents on the steel side, and of a ternary Fe-Al-Si compound on the weld side.

Whatever the loading, the failure of the lap assemblies initiates systematically in the weld root, then propagates along the interface and/or in the weld.

The monotonic shear-tensile strength of the assemblies is mainly determined by the size of the porosities formed in the weld root, and can reach ~75% of the strength of the aluminum base material when the mean power is reduced and the welding speed is high.

The cyclic tensile behavior of the assemblies is more complex. If the large porosities formed in the weld root at low welding speeds produce the same effect as in monotonic tensile test, by reducing the lifetime of the assemblies, an excessive increase in the welding speed reduces the lifetime under cyclic loading.

The lifetime of the assemblies under cyclic tensile loading can exceed 10^4 cycles for a maximal linear force of 98 $N.mm^{-1}$, and 10^7 cycles for a maximal linear force of 42 $N.mm^{-1}$.

Acknowledgements

The authors are grateful to the Erasmus Mundus program for financial support.

References

Borrisutthekul, R., Yachi, T., Miyashita, Y., Mutoh, Y., 2007. Suppression of intermetallic reaction layer formation by controlling heat flow in dissimilar joining of steel and aluminum alloy. Mater. Sc. Engineer. A467, 108-113.

Bouayad, A., Gerometta, C., Belkebir, A., Ambari, A., 2003. Kinetic interactions between solid iron and molten aluminium. Mater. Sc. Engineer. A363, 53–61.

Bouché, K., Barbier, F., Coulet, A., 1998. Intermetallic compound layer growth between solid iron and molten aluminium. Mater. Sc. Engineer. A249, 167-175.

Cao, R., Yu, G., Chen, J.H., Wang, P.C., 2013. Cold metal transfer joining aluminum alloys-to-galvanized mild steel. J. Mater. Process. Technol. 213, 1753–1763.

Chen, Y.C., Gholinia, A., Prangnell, P.B., 2012. Interface structure and bonding in abrasion circle friction stir spot welding: A novel approach for rapid welding aluminium alloy to steel automotive sheet. Mater. Chem. Phys. 134, 459– 463.

Cheng, W., Wang, C., 2011. Effect of silicon on the formation of intermetallic phases in aluminide coating on mild steel. Intermetallics. 19, 1455-1460.

Coelho, R.S., Kostka, A., Dos Santos, J.F., Kaysser-Pyzalla, A., 2012. Friction-stir dissimilar welding of aluminium alloy to high strength steels: Mechanical properties and their relation to microstructure. Mater. Sc. Engineer. A556, 175–183.

Dharmendra, C., Rao, K.P., Wilden, J., Reich, S., 2011. Study on laser welding–brazing of zinc coated steel to aluminum alloy with a zinc-based filler. Mater. Sc. Engineer. A528, 1497–1503.

Dong, H., Yang, L., Dong, C., Kou, S., 2012a. Improving arc joining of Al to steel and Al to stainless steel. Mater. Sc. Engineer. A534, 424– 435.

Dong, H., Hu, W., Duan, Y., Wang, X., Dong, C. 2012b. Dissimilar metal joining of aluminium alloy to galvanized steel with Al-Si, Al-Cu, Al-Si-Cu and Zn-Al filler wires. J. Mater. Process. Technol. 212, 458–464.

Fan, J., Thomy. C., Vollertsen, F., 2011. Effect of thermal cycle on the formation of intermetallic compounds in laser welding of aluminum-steel overlap joints. Phys. Procedia. 12, 134-141.

Kobayashi, S., Yakou, T., 2002. Control of intermetallic compound layers at interface between steel and aluminum by diffusion-treatment. Mater. Sc. Engineer. A338, 44-53.

Kore, S.D., Date, P.P., Kulkarni, S.V., 2008. Electromagnetic impact welding of aluminum to stainless steel sheets. J. Mater. Process. Technol. 208, 486–493.

Lin, S.B., Song, J.L., Yang, C.L., Fan, C.L., Zhang, D.W., 2010. Brazability of dissimilar metals tungsten inert gas butt welding–brazing between aluminum alloy and stainless steel with Al–Cu filler metal. Mater. Des. 31, 2637–2642.

Lin, J., Mab, N., Lei, Y., Murakawa, H., 2013. Shear strength of CMT brazed lap joints between aluminum and zinc-coated steel. J. Mater. Process. Technol. 213, 1303–1310.

Mathieu, A., Pontevicci, S., Viala, J., Cicala, E., Matteï, S., Grevey, D., 2006. Laser brazing of a steel/aluminium assembly with hot filler wire (88% Al, 12% Si). Mater. Sc. Engineer. A435-436, 19-28.

Mathieu, A., Shabadi, R., Deschamps, A., Suery, M., Mattei, S., Grevey, D., Cicala, E., 2007. Dissimilar material joining using laser (aluminum to steel using zinc-based filler wire). Optics and Laser Technology. 39, 652–661.

Mezrag, B., Deschaux-Beaume, F., Benachour, M., 2015. Control of mass and heat transfer for steel/aluminium joining using Cold Metal Transfer process. Sc. Technol. Weld. Join. 20, 189-198.

Peyre, P., Sierra, G., Deschaux-Beaume, F., Stuart, D., Fras, G., 2007. Generation of aluminium–steel joints with laser-induced reactive wetting. Mater. Sc. Engineer. A. 444, 327–338.

Raghavan, V., 2009. Phase diagram evaluations Al-Fe-Si (Aluminum-Iron-Silicon). J. Phase Equilibria and Diffusion. 2 ; 1547–7037.

Shahverdi, H.R., Ghomashchi, M.R., Shabestari, S., Hejazi, J., 2002. Microstructural analysis of interfacial reaction between molten aluminum and solid iron. J. Mater. Process. Technol. 124, 345-352.

Sierra, G., Peyre, P., Deschaux-Beaume, F., Stuart, D., Fras, G., 2007. Steel to aluminium key-hole laser welding. Mater. Sc. Engineer. A447, 197–208.

Sierra, G., Peyre, P., Deschaux-Beaume, F., Stuart, D., Fras, G., 2008a. Galvanised steel to aluminium joining by laser and GTAW processes. Mater. Charac. 59, 1705–1715.

Sierra, G., Peyre, P., Deschaux-Beaume, F., Stuart, D., Fras, G., 2008b. Steel to aluminium braze welding by laser process with Al–12Si filler wire. Sc. Technol. Weld. Join. 13, 430-437.

Song, J.L., Lin, S.B., Yang, C.L., Ma, G.C., Liu, H., 2009a. Spreading behavior and microstructure characteristics of dissimilar metals TIG welding–brazing of aluminum alloy to stainless steel. Mater. Sc. Engineer. A509, 31–40.

Song, J.L., Lin, S.B., Yang, C.L., Fan, C.L., 2009b. Effects of Si additions on intermetallic compound layer of aluminum–steel tig welding–brazing joint. Mater. Sc. Engineer. 488, 217-222.

Springer, H., Kostka, A., Payton, E.J., Raabe, D., Kaysser-Pyzalla, A., Eggeler, G., 2011. On the formation and growth of intermetallic phases during interdiffusion between low-carbon steel and aluminum alloys. Acta Mater. 59, 1586–1600.

Torkamany, M.J., Tahamtan, S., Sabbaghzadeh, J., 2010. Dissimilar welding of carbon steel to 5754 aluminum alloy by Nd:YAG pulsed laser. Mater. Des. 31, 458–465.

Watanabe, T., Takayama, H., Yanagisawa, A., 2006. Joining of aluminum alloy to steel by friction stir welding. J. Mater. Process. Technol. 178, 342–349.

Watanabe, T., Sakuyama, H., Yanagisawa, A., 2009. Ultrasonic welding between mild steel sheet and Al–Mg alloy sheet. J. Mater. Process. Technol. 209, 5475–5480.

Yan, S., Hong, Z., Watanabe, T., Jingguo, T., 2010. CW/PW dual-beam YAG laser welding of steel/aluminum alloy sheets. Optics Lasers Engineer. 48, 732–736.

Yang, S., Zhang, J., Lian, J., Lei, Y., 2013. Welding of aluminum alloy to zinc coated steel by cold metal transfer. Mater. Des. 49, 602–612.

Zhang, H.T., Feng, J.C., He, P., Hackl, H., 2007. Interfacial microstructure and mechanical properties of aluminium–zinc-coated steel joints made by a modified metal inert gas welding–brazing process. Mater. Charac. 58, 588–592.

Zhang, H., Liu, J., 2011. Microstructure characteristics and mechanical property of aluminum alloy/stainless steel lap joints fabricated by MIG welding–brazing process. Mater. Sc. Engineer. A528, 6179–6185.

Zhang, M.J., Chen, G.Y., Zhang, Y., Wu, K.R., 2013. Research on microstructure and mechanical properties of laser keyhole welding–brazing of automotive galvanized steel to aluminum alloy. Mater. Des. 45, 24–30.

Zhou, Y., Lin, Q., 2014. Wetting of galvanized steel by Al 4043 alloys in the first cycle of CMT process. J. alloys compounds. 589, 307-313.